












Stormy Weather in 3C 196.1: Nuclear Outbursts and Merger Events Shape the Environment of the Hybrid Radio Galaxy 3C 196.1

F. Ricci^{1,2,3} , L. Lovisari¹ , R. P. Kraft¹ , F. Massaro^{4,5} , A. Paggi⁴ , E. Liuzzo⁶, G. Tremblay¹ , W. R. Forman¹ ,
S. Baum^{7,8}, C. O’Dea^{7,9} , and B. Wilkes¹ 

¹ Smithsonian Astrophysical Observatory, 60 Garden Street, Cambridge, MA 02138, USA; riccif@fis.uniroma3.it

² Instituto de Astrofísica and Centro de Astroingeniería, Facultad de Física, Pontificia Universidad Católica de Chile, Casilla 306, Santiago 22, Chile

³ Dipartimento di Matematica e Fisica, Università Roma Tre, via della Vasca Navale 84, I-00146 Roma, Italy

⁴ Dipartimento di Fisica, Università degli Studi di Torino, via Pietro Giuria 1, I-10125 Torino, Italy

⁵ Consorzio Interuniversitario per la Fisica Spaziale (CIFS), via Pietro Giuria 1, I-10125, Torino, Italy

⁶ Istituto di Radioastronomia, INAF, via Gobetti 101, I-40129, Bologna, Italy

⁷ University of Manitoba, Department of Physics and Astronomy, Winnipeg, MB R3T 2N2, Canada

⁸ Center for Imaging Science, Rochester Institute of Technology, 84 Lomb Memorial Drive, Rochester, NY 14623, USA

⁹ School of Physics and Astronomy, Rochester Institute of Technology, 84 Lomb Memorial Drive, Rochester, NY 14623, USA

Received 2018 April 24; revised 2018 September 18; accepted 2018 September 24; published 2018 October 29

Abstract

We present a multiwavelength analysis based on archival radio, optical, and X-ray data of the complex radio source 3C 196.1, whose host is the brightest cluster galaxy of a $z = 0.198$ cluster. *HST* data show $H\alpha + [N II]$ emission aligned with the jet 8.4 GHz radio emission. An $H\alpha + [N II]$ filament coincides with the brightest X-ray emission, the northern hotspot. Analysis of the X-ray and radio images reveals cavities located at galactic and cluster scales. The galactic-scale cavity is almost devoid of 8.4 GHz radio emission and the southwestern $H\alpha + [N II]$ emission is bounded (in projection) by this cavity. The outer cavity is cospatial with the peak of 147 MHz radio emission, and hence we interpret this depression in X-ray surface brightness as being caused by a buoyantly rising bubble originating from an active galactic nuclei outburst ~ 280 Myr ago. A *Chandra* snapshot observation allowed us to constrain the physical parameters of the cluster, which has a cool core with a low central temperature ~ 2.8 keV, low central entropy index ~ 13 keV cm^2 and a short cooling time of ~ 500 Myr, which is < 0.05 of the age of the universe at this redshift. By fitting jumps in the X-ray density, we found Mach numbers between 1.4 and 1.6, consistent with a shock origin. We also found compelling evidence of a past merger, indicated by a morphology reminiscent of gas sloshing in the X-ray residual image. Finally, we computed the pressures, enthalpies E_{cav} and jet powers P_{jet} associated with the cavities: $E_{\text{cav}} \sim 7 \times 10^{58}$ erg, $P_{\text{jet}} \sim 1.9 \times 10^{44}$ erg s^{-1} for the inner cavity and $E_{\text{cav}} \sim 3 \times 10^{60}$ erg, $P_{\text{jet}} \sim 3.4 \times 10^{44}$ erg s^{-1} for the outer cavity.

Key words: galaxies: active – galaxies: clusters: general – galaxies: clusters: intracluster medium – radio continuum: galaxies – radio continuum: ISM – X-rays: galaxies: clusters

1. Introduction

Nuclear outflows from active galactic nuclei (AGNs) have a dramatic impact on cosmic structure formation and evolution. These energetic outflows are invoked to explain the anti-hierarchical quenching of star formation in massive galaxies, the exponential cutoff at the bright end of the galaxy luminosity function, the black-hole-host scaling relations and the quenching of cooling flows in cluster cores (e.g., Begelman & Nath 2005; Scannapieco et al. 2005; Main et al. 2017). The mutual radio galaxy/cluster interaction is significant for both: the intracluster medium (ICM) can change the jet propagation, while the great mechanical power of radio AGNs can quench cooling in cluster cool cores.

One of the most important *Chandra* results in cluster science is the discovery of X-ray cavities and shocks (e.g., see reviews from McNamara & Nulsen 2007; Gitti et al. 2012), which are the smoking guns of the so-called radio- (or kinetic-, maintenance-) mode feedback (Birzan et al. 2008; Cavagnolo et al. 2010; for a review see Fabian 2012) of AGNs, which are fed by the accretion of circumnuclear gas (e.g., Gaspari et al. 2015). The AGN energy released by the accretion process heats up or sweeps out the surrounding medium, reducing the accretion rate onto the black hole until it is switched off. When the gas cools down or is replenished, e.g., through a merger

with another galaxy, accretion can start again. The new episode of accretion can eventually trigger the radio jets, closing the feedback loop.

The radio-mode feedback has been observed in cool core clusters (MS0735.6+7421 McNamara et al. 2009; A2052 Blanton et al. 2011; A2597 Tremblay et al. 2012; M87 Forman et al. 2017), in groups (e.g., NGC 5813 Randall et al. 2015), and in isolated ellipticals (e.g., NGC 4636 Jones et al. 2002) where the ICM is heated up by AGN jet-inflated plasma bubbles that buoyantly rise in the hot, X-ray emitting atmosphere (Churazov et al. 2013; Su et al. 2017, see also Boehringer et al. 1993; Churazov et al. 2000, 2001 for the first *ROSAT* measurements in Perseus and Virgo). As the bubbles rise, their energy is converted into motions of the X-ray emitting plasma that, eventually, is converted into thermal energy.

Our group has conducted over the last 8 years a *Chandra* snapshot survey (see Massaro et al. 2010, 2012, 2013, 2015, 2018; Stuardi et al. 2018) aimed at characterizing the X-ray radiation from jets, hotspots, nuclei, and cluster emission of the most powerful, and probably most studied, radio galaxies known, the Third Cambridge Revised catalog (3CR; Bennett 1962; Spinrad et al. 1985).

Our *Chandra* snapshot program allowed us to select targets for detailed analysis. 3C 196.1 is very promising: it is a hybrid

morphology (both FR I and FR II; Fanaroff & Riley 1974) radio galaxy embedded in a $kT \sim 4$ keV galaxy cluster and has convincing morphological signatures of radio galaxy/cluster interaction (Massaro et al. 2012), with structures in the X-ray clearly related to ongoing and past outbursts of the radio galaxy.

3C 196.1 lies at $z = 0.198$ within a cluster of galaxies CIZA J0815.4-0308 observed by *ROSAT* (Kocevski et al. 2007). 3C 196.1 has been classified in the optical as a low-excitation radio galaxy (LERG; Buttiglione et al. 2010), and is associated with the brightest cluster galaxy (BCG), an elliptical cD galaxy, the dominant galaxy of a group of 14 others that lie within about 350 kpc from its core (Baum et al. 1988). Madrid et al. (2006) show that its near-infrared image is elliptical, presenting an elongated structure NE to SW, in the same direction as the inner scale jet. The same morphology is seen in the optical (Baum et al. 1988; de Koff et al. 1996). The optical color gradients of 3C 196.1 show periodic shells that could reflect merging and galactic cannibalism (Zirbel 1996). The host galaxy has optical isophotes whose centroids clearly shift to the SW at small radii (de Koff et al. 1996). This suggests that a merger has occurred several dynamical times ago. In fact, stellar tidal debris from a merger wash out over a few dynamical times, while shells in stellar surface brightness, which can manifest as isophote centroid offsets, can be long-lived remnants.

In this work, we investigate the physical conditions of the 3C 196.1 environment in order to shed light on ongoing interaction between the AGN and surrounding medium. We present a multiwavelength study based on radio, optical, and X-ray archival data of 3C 196.1, aimed at investigating the morphology and the nature of the multiphase emitting gas, unveil the impact of past AGN outbursts, and dissect merger signatures. The paper is organized as follows: In Section 2, radio, optical, and X-ray archival data are presented. Section 3 describes the X-ray analysis, with imaging presented in Section 3.1, spectral analysis carried out in Section 3.2, and surface brightness profiles extracted and fitted in Section 3.3. In Section 3.4, we adopted two edge-enhancement methods to localize small-amplitude wiggles in the surface brightness. In Section 4, the results are presented and finally Section 5 is devoted to a summary and conclusions. We assumed a flat cosmology with $H_0 = 72 \text{ km s}^{-1} \text{ Mpc}^{-1}$, $\Omega_M = 0.27$, and $\Omega_\Lambda = 0.73$ (Dunkley et al. 2009). This means that for 3C 196.1, the angular scale is $3.197 \text{ kpc arcsec}^{-1}$ and the luminosity distance is 946 Mpc. For all the figures presented in this work, the standard astronomical orientation is adopted, i.e., north up and east to the left.

2. Data

2.1. Radio Data

We used high-frequency 8.4 GHz Very Large Array (VLA) archival data to investigate the core region of the galaxy, whereas we used low-frequency 147 MHz Giant Meterwave Radio Telescope (GMRT) archival data to study the diffuse emission in the cluster outskirts (~ 500 kpc, i.e., $\sim 0.5 R_{500}^{10}$). These radio frequencies sample different spatial scales due to the angular resolution that each radio band can achieve. The high-frequency 8.4 GHz VLA data shown in Figure 1 (left

panel, contours on top of the optical image) has been observed on 1995 July 2 with the VLA in configuration A, the restoring beam is $(0''.3 \times 0''.3, 0^\circ)$, the rms is $9.13 \times 10^{-2} \text{ mJy/beam}$ and the brightest peak is at $\sim 1.37 \times 10^{-2} \text{ Jy/beam}$. The 8.4 GHz flux of the NE (SW) radio lobe is 71 (32) mJy.

The 147 MHz GMRT data has been retrieved from the TIFR GMRT Sky Survey Alternative Data Release (TGSS ADR; Intema et al. 2017) website.¹¹ The TGSS ADR ID number is R26D31 and is a mosaic image of 5 deg square. The 147 MHz emission contours are superposed on the X-ray emission in Figure 2 (right panel, black contours). The restoring beam is $(26''.96 \times 25'', 0^\circ)$, the rms is 0.13 mJy/beam and the brightest peak is at $\sim 16.9 \text{ Jy/beam}$. The radio flux of the SW diffuse emission is 0.264 Jy at 147 MHz.

2.2. HST Observation

The optical archival data were observed on 2006 December 3 during Cycle 15 with the Advanced Camera for Surveys (ACS) on board *HST*, snapshot program 10882 (PI: Sparks), originally published by Tremblay et al. (2009, we refer the reader to this work for details on data reduction and calibration). The narrowband ACS ramp filter F782N was used to trace the restframe optical $\text{H}\alpha + [\text{N II}]$ emission line complex. The *HST* data have been continuum subtracted to isolate the $\text{H}\alpha + [\text{N II}]$ emission. In Figure 1, we report the central part of the radio galaxy 3C 196.1 imaged with *HST*/ACS with the high-frequency radio emission at 8.4 GHz superimposed (cyan contours). The *HST* image was registered in order to align the optical isophotal peak with the southern jet component. The shift of the *HST* image was $\lesssim 1''.2$. The overall $\text{H}\alpha + [\text{N II}]$ emission spans ~ 10 kpc projected distance, inside the galaxy, starting from the core and extending along the radio jet. The $\text{H}\alpha + [\text{N II}]$ emission is aligned with the 8.4 GHz radio emission. Similar alignments of radio with optical emission lines have been observed in many radio galaxies. This is known as the ‘‘alignment effect’’: in powerful radio galaxies, the optical line emitting gas ($T \sim 10^4 \text{ K}$) in the proximity of the nuclei has been found to be spatially aligned with the radio jet axes on kiloparsec-scales (Fosbury 1986; Hansen et al. 1987; Baum et al. 1988, 1990; de Vries et al. 1999; Tremblay et al. 2009). The alignment effect is generally explained as due to shocks induced by the jet propagation and by AGN photoionization (Baum & Heckman 1989; Dopita & Sutherland 1995, 1996; Best et al. 2000).

There is also a filament to the NE that drapes across the northern radio lobe. This filamentary structure is not seen in $[\text{O III}]$, which shows high-excitation emission in two localized hotspots cospatial with the elongated bright core (see Figure 7 in Tremblay et al. 2009).

2.3. Chandra Observation

3C 196.1 was observed during *Chandra* AO12, OBSID 12729 on 2011 February 11, with a nominal 8 ks exposure. The ACIS-S back-illuminated chip was used in VERY FAINT MODE with standard frame times (3.2 s). The source was positioned on ACIS-S3. Data reduction has been performed following the standard reduction procedure described in the *Chandra* Interactive Analysis of Observations (CIAO, Fruscione et al. 2006) threads,¹² using CIAO v4.9 and the *Chandra* CalDB version 4.7.4. Level 2

¹⁰ R_{500} defines the radius at which the overdensity is equal to 500 times the critical density of the universe at the cluster redshift.

¹¹ <http://tgssadr.strw.leidenuniv.nl/doku.php>

¹² <http://cxc.harvard.edu/ciao/guides/index.html>

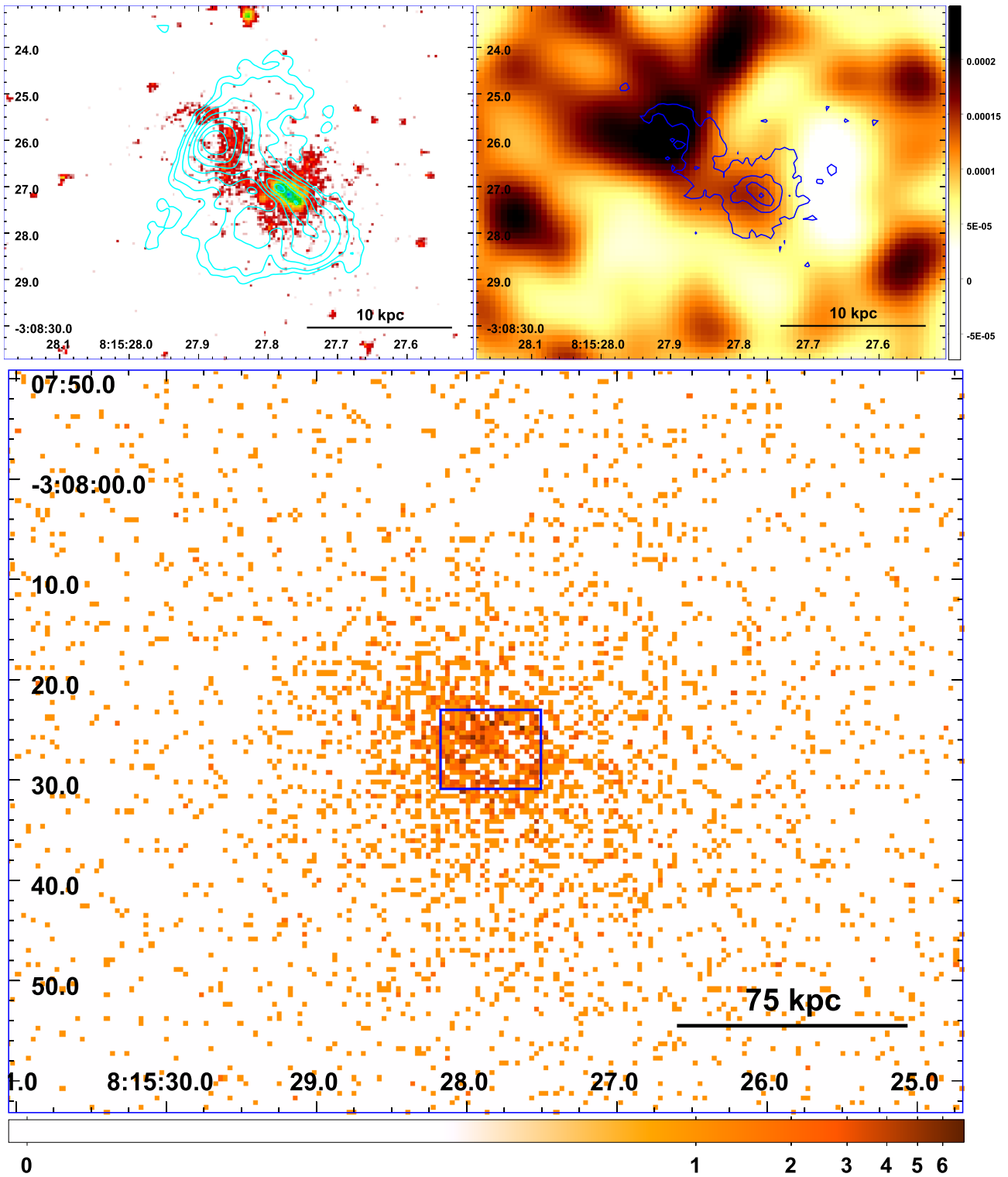


Figure 1. Images of the central BCG 3C 196.1 and of the surrounding cluster and ICM. Top panels show the nuclear region of 3C 196.1 and share the same scale, with an FoV of $\sim 10 \times 8$ arcsec² (i.e., $\sim 30 \times 25$ kpc²). Top left: *HST*/*ACS* observation of 3C 196.1 from Tremblay et al. (2009), with 8.4 GHz VLA contours superimposed. The *HST* data have been continuum subtracted, to show only the H α + $[\text{N II}]$ emission. The 8.4 GHz contours start at $\sim 3\sigma$, i.e., 0.275 mJy, and increase with a square-root scale; the clean beam is ($0''.3 \times 0''.3$, 0°). The H α + $[\text{N II}]$ emission has been aligned with the 8.4 GHz VLA data (shift $\lesssim 1''/2$, see the text for details). An H α + $[\text{N II}]$ filament extends across the NE radio lobe. The H α + $[\text{N II}]$ is aligned with the radio emission (so-called alignment effect, e.g., Baum et al. 1988). Top right: the *Chandra* 0.7–2 keV emission is shown with the H α + $[\text{N II}]$ contours superimposed. No shift was applied to align the images. The *Chandra* data have $0''.123$ pixel scale and have been smoothed with a Gaussian kernel of $1''$. Depressions in surface brightness are in white. The H α + $[\text{N II}]$ contours start at 0.378×10^{-19} erg s⁻¹ cm⁻² Å⁻¹ and increase with a square-root scale. The SW H α + $[\text{N II}]$ emission is bounded to the W, S, and SE by regions of low X-ray surface brightness. Bottom: the 0.5–10 keV *Chandra* image, showing an FoV of $\sim 93 \times 73$ arcsec² (i.e., $\sim 297 \times 234$ kpc²), with native pixel size. The blue box at the center marks the region of 3C 196.1 shown in the top panels. The logarithmic color scale shows the counts per pixel.

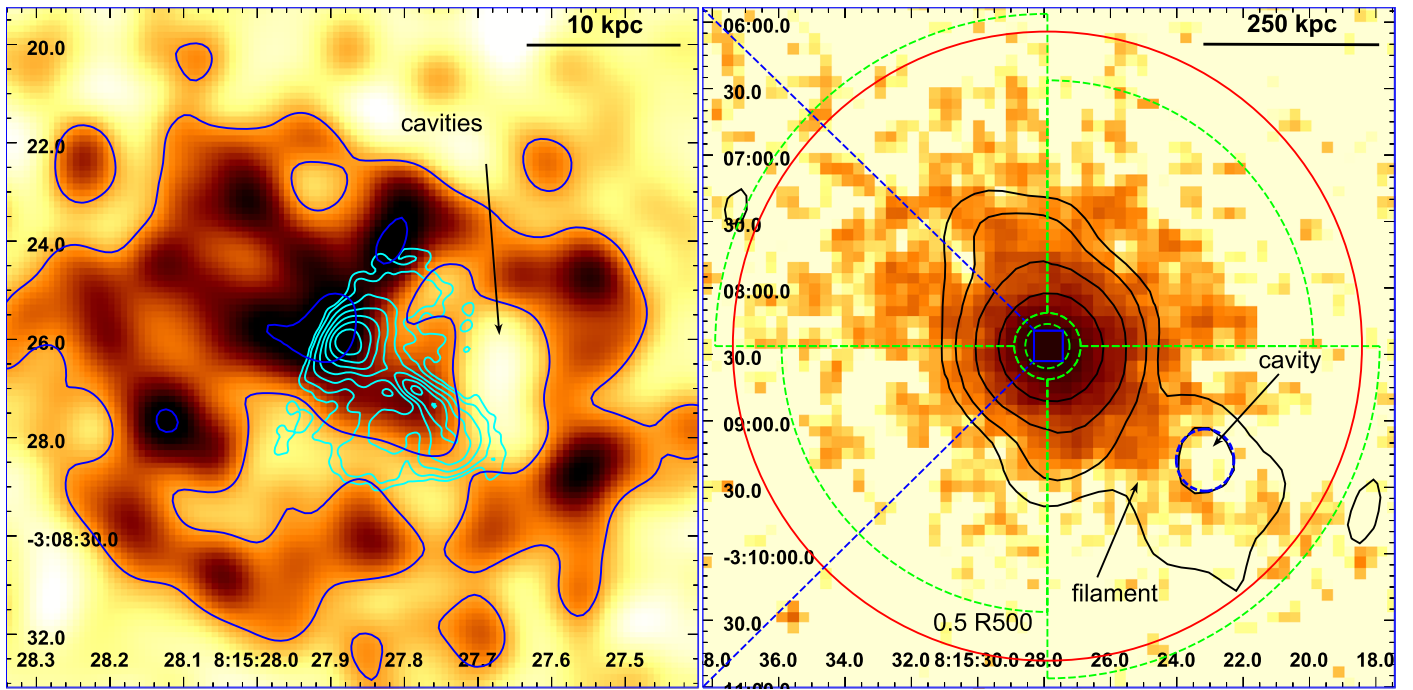


Figure 2. *Chandra* 0.7–2 keV energy filtered and point sources subtracted images of the central BCG 3C 196.1 and of the surrounding cluster and ICM. Regions of low surface brightness are in white. Left: inner $\sim 13 \times 14$ arcsec² (i.e., $\sim 44 \times 45$ kpc²) of the BCG, centered on the brightest X-ray peak. The image is shown with a $0''.123$ pixel size and has been smoothed with a $1''$ Gaussian. VLA 8.4 GHz contours are overlaid in cyan (for details, see Figure 1), while the X-ray contours are shown in blue. The lowest blue contour encloses a region of low surface brightness, a “butterfly-shaped” cavity (marked with a black arrow). The brightest X-ray peak is cospatial with the northern radio lobe and could be a hotspot. Right: the BCG and the cluster are shown up to the outskirts, with an FoV of $\sim 5 \times 5$ arcmin² (i.e., $\sim 960 \times 960$ kpc²). Pixel size is $5''$, Gaussian smoothing with FWHM = $5''$. The central blue box is $\sim 13 \times 14$ arcsec² and contains the zoom in shown in the left panel. GMRT 147 MHz contours are overlaid in black starting at $\sim 3\sigma$, i.e., 39 mJy with a logarithmic scale. The clean beam is $(26''.96 \times 25'', 0^\circ)$. The arrow marks a large filament that has a projected extension of $\sim 2'$ (i.e., ~ 384 kpc). It may also be the bottom of a large cavity (highlighted by the dashed blue ellipse), which is cospatial with the peak of the SW low-frequency diffuse emission. The red circle shows the estimated $0.5R_{500}$. Extraction regions used in Section 3.2 are shown with green dashed lines.

event files were generated using the `chandra_repro` task. Events were filtered for grades 0, 2, 3, 4, and 6. The light curve was extracted and checked for high background intervals, the actual live time is 7.93 ks. The resulting 0.5–10 keV *Chandra* image in photon counts with native pixel size is shown in the bottom panel of Figure 1, in order to show the structures in the original data without any Gaussian smoothing or image processing.

3. X-Ray Analysis

3.1. Imaging

Figure 2 presents the diffuse X-ray emission in the energy range 0.7–2 keV, with pixel size $0''.123$ (left) and $5''$ (right). Point sources were detected with the CIAO task `wavdetect` (with 1, 2, 4, 8, 16, and 32 pixels sequence of wavelet scales), adopting a probability of spurious detection of 10^{-6} , and then replaced with local background. Five point sources were detected, all located outside the regions considered in our subsequent analysis. Thus, our results are not affected by the removal of point sources. The images have been smoothed with a Gaussian kernel of $1''$ (left) and $5''$ (right). The left panel of Figure 2 shows the central $\sim 44 \times 45$ kpc² region together with 8.4 GHz contours (cyan) and X-ray contours (blue). The radio source is oriented along the steepest gradient in the X-ray emission. The X-ray surface brightness is complex and is not symmetric, extended along a position angle PA¹³ $\sim 40^\circ$ that

matches the optical major axis of the BCG stellar isophotes (see Figure 32 in de Koff et al. 1996). The image shows the presence of sharp surface brightness edges in the central regions of the cluster. The lowest blue contour marks a system of “butterfly-shaped” surface brightness deficits (see the black arrow in Figure 2), also reported by Massaro et al. (2012) as a “ghost cavity”. The southern jet of the 8.4 GHz source (cyan contours) is bounded (in projection) to the W and E by these “butterfly-shaped” deficits of X-ray radiation. This cavity is mostly devoid of high-frequency radio emission. The best description of this source with the available $0''.3$ resolution is an *hymor* (hybrid morphology radio source Gopal-Krishna & Wiita 2000). The SW side is jet-like (i.e., FR I) whereas the NE side appears to be a classical FR II lobe with a brightness enhancement toward the edge, the X-ray peak marking the location where the NE jet impacts the higher density ICM. Several radio sources have been observed to exhibit a mixed morphology (Kaiser & Best 2007; Kharb et al. 2010; Kapińska et al. 2017), suggesting the FR I/II dichotomy is at least partly due to environmental effects.

On the central panel of Figure 1 the central region is further magnified, with a field of view (FoV) of $\sim 30 \times 25$ kpc². The $H\alpha + [N II]$ emission is overlaid with blue contours. No shift was applied to register the *Chandra* and *HST* images. The SW optical line emission appears to be confined by the butterfly-shaped X-ray cavity. The $H\alpha + [N II]$ NE filamentary emission is cospatial with the northern hotspot.

Also at larger scales, the diffuse X-ray emitting gas distribution is asymmetric, elongated northeast to southwest,

¹³ Positive direction is counterclockwise north through east.

Table 1
Results of the Spectral Fitting Analysis of the 0.5–7 keV *Chandra* Data

Region ($r_{\text{in}}, r_{\text{out}}$) (1)	N (2)	kT (keV) (3)	Z (Z_{\odot}) (4)	APEC norm (10^{-3} cm^{-5}) (5)	χ^2_{ν} (6)
core 0 [0, 10'']	1115	2.88 ± 0.19 2.81 ± 0.22	0.80 ± 0.24 0.3 ^a	1.090 ± 0.090 1.297 ± 0.046	0.99(44) 1.13(45)
core 1 [0, 15'']	1534	3.18 ± 0.17 3.14 ± 0.21	0.98 ± 0.23 0.3 ^a	1.406 ± 0.097 1.718 ± 0.053	0.93(57) 1.16(58)
NW [15'', 2']	809	5.23 ± 0.99 5.24 ± 0.97	0.24 ± 0.35 0.3 ^a	0.791 ± 0.075 0.781 ± 0.036	1.00(33) 0.97(34)
NE [15'', 2/5]	959	5.15 ± 0.82 4.85 ± 0.88	1.12 ± 0.65 0.3 ^a	0.714 ± 0.080 0.833 ± 0.038	0.98(39) 1.02(40)
SE [15'', 2']	590	4.66 ± 0.92 4.37 ± 0.94	0.99 ± 0.86 0.3 ^a	0.399 ± 0.063 0.462 ± 0.027	1.20(25) 1.20(26)
SW [15'', 2/5]	1194	7.63 ± 1.80 7.46 ± 1.68	0.16 ± 0.35 0.3 ^a	0.975 ± 0.078 0.956 ± 0.035	0.97(50) 0.95(51)
All [0, 2']	4228	4.24 ± 0.24 4.25 ± 0.27	0.73 ± 0.14 0.3 ^a	4.01 ± 0.14 4.412 ± 0.084	1.10(154) 1.16(155)

Notes. The XSPEC model used is `phabs × APEC`, with the N_{H} column fixed to Galactic value and z fixed to 0.198. Prior to extraction, the data were filtered for flaring events, and compact point sources were removed. Spectra were rebinned using a 20-count threshold. Symmetric 1σ confidence intervals are shown on fit parameters. Columns are as follows: (1) extraction region, with range [$r_{\text{in}}, r_{\text{out}}$], centered at R.A._{J2000} = 8:15:27.900 and decl._{J2000} = −3:08:26.265 (see Figure 2); (2) net-counts; (3) the best-fit temperature of the APEC model in keV units; (4) the abundance, in solar units; (5) the APEC normalization; (6) the reduced chi-square χ^2_{ν} , with the degrees of freedom ν in parentheses.

^a Parameter has been frozen.

as shown in the right panel of Figure 2, where the system is imaged up to $\sim 0.5R_{500}$, with an FoV of $\sim 1 \times 1 \text{ Mpc}^2$. The image shows that the peak of the X-ray emission is centered on the BCG and that there is a gradient in the surface brightness distribution, with the lowest surface brightness region extending up to few hundreds of kiloparsecs. Right panel of Figure 2 presents low-frequency 147 MHz GMRT contours in black. The peak of the low-frequency 147 MHz emission (in the SW extension) is cospatial with a region of low X-ray surface brightness (see dashed blue ellipse), that could be a large cavity filled with a low-frequency radio bubble. In the outer region there is an X-ray filament (see black arrow) that has a projected extension of $\sim 2'$, corresponding to $\sim 384 \text{ kpc}$. It may also outline the southern border of the aforementioned large cavity.

To further explore the underlying physical state of the gas, we derive the temperature in both the nuclear region and the cluster outskirts in Section 3.2, and we analyze the surface brightness profiles in Section 3.3.

3.2. Spectral Analysis

We performed a temperature analysis of the cluster, from the inner core up to $\sim 0.5R_{500}$. First, we analyzed the central core, considering two circles of radius $r = 10''$ and $15''$, both centered on the centroid of the X-ray emission (R.A._{J2000} = 8:15:27.900 and decl._{J2000} = −3:08:26.265). These two central regions are called *core 0* and *core 1* in Table 1. We then analyzed the cluster by dividing the emission into four sectors evenly spanning the 360°. The radial extents of these four regions are $15''\text{--}2'$ for the NW and SE sectors (since in the SE direction the S3 chip ends at that radius) and $15''\text{--}2/5$ in the NE and SW sectors (see the six green dashed regions in the right panel of Figure 2). We also considered the whole region within $r = 2'$ to derive the global temperature.

We extracted the spectra in these regions using the CIAO task `specextract`, thereby automating the creation of count-weighted response matrices. Background correction was taken into account using the proper blank sky field event file, which was created using the CIAO task `blanksky`. Background spectra were extracted from the blank sky observation that was reprojected to match the observation. The background-subtracted spectra were then filtered in energy between 0.5 and 7 keV, binned using a 20 count threshold and fit using iterative χ^2 minimization techniques with `xspec` version 12.9.1 (Arnaud 1996).

The model adopted is `phabs × APEC` with column density fixed to the Galactic value $N_{\text{H}} = 5.81 \times 10^{20} \text{ cm}^{-2}$. We fitted each region twice, first leaving the abundance free to vary and then fixing it to 0.3 times the solar value, which is often found in cluster atmospheres (see, e.g., Owers et al. 2009). Abundances were computed taking as reference the solar metallicity as reported by Asplund et al. (2009). Best-fit values are listed in Table 1.

3.3. Surface Brightness Profiles

We extracted surface brightness profiles by considering an azimuthal area up to $r = 2'$ and again in four sectors with outer radii $2'$ (NW and SE) or $2/5$ (NE and SW). All five regions were spanned by $3''$ wide radial bins, apart from the inner core region (up to $10''$), which was divided into $1''$ -wide bins. In the surface brightness profile analysis, the *Chandra* event file was filtered in energy between 0.7 and 2 keV band, which is less sensitive to the gas temperature. It was then exposure-corrected, background-subtracted, and bright point sources were excluded. The same point sources area was also removed from the blank sky field. Monochromatic exposure maps were computed with nominal energies of 1.35 keV. The background-subtracted and exposure-corrected radial profiles are shown in Figure 3.

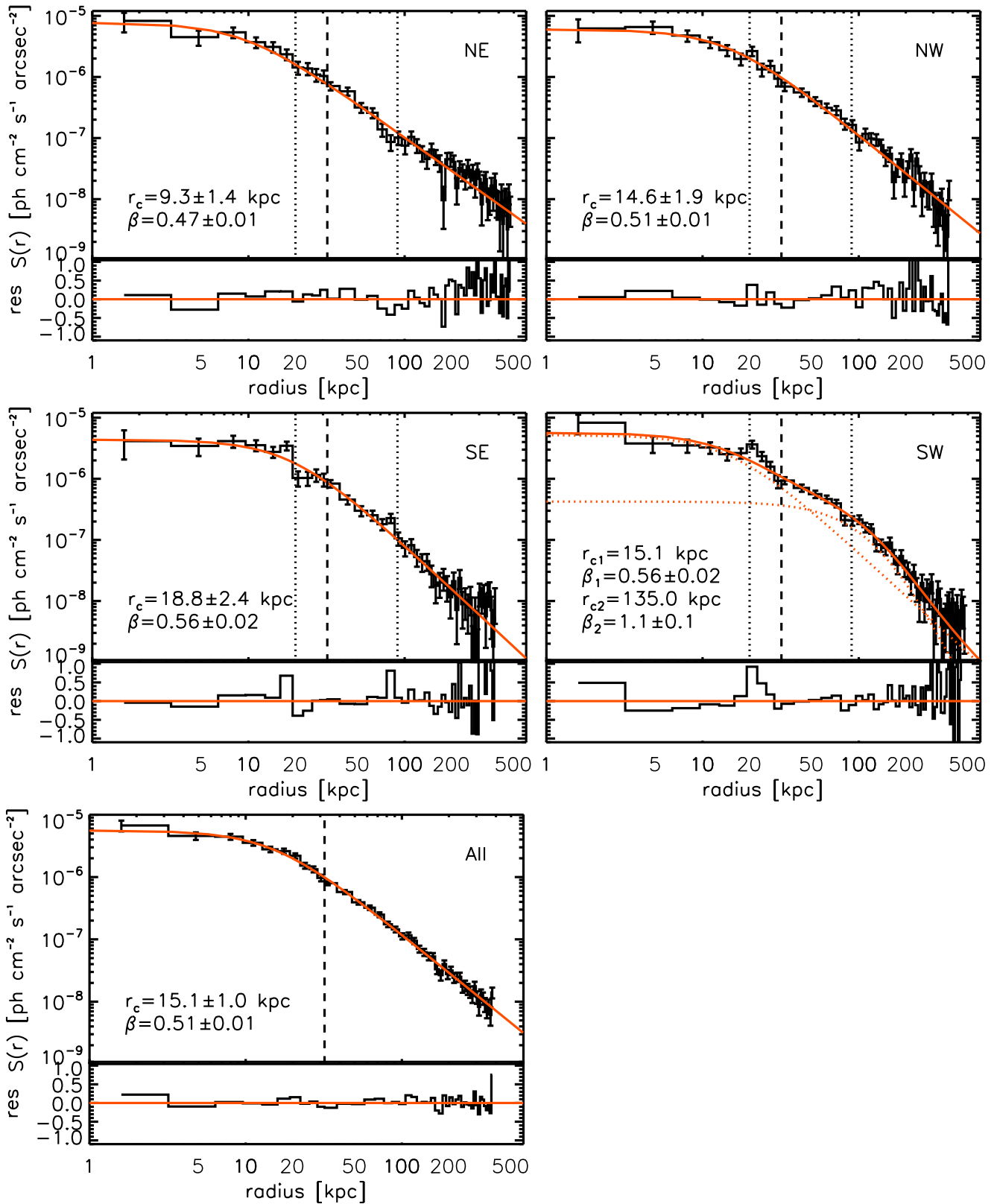


Figure 3. Exposure-corrected and background-subtracted surface brightness profiles of four sectors, evenly spanning the 360° , and of an azimuthal region, extending up to $2'$. Bright point sources were excluded. Radial bins are $3''$ wide, with the exception of the inner $10''$, which were spanned by $1''$ -bins. The radial profiles have been computed in the $0.7\text{--}2$ keV band, which is less sensitive to the temperature. Parameters of the β -models are also reported. The dashed line marks the inner core region $r = 10''$, which has a lower temperature of ~ 3 keV (see region *core 0* in Table 1). The dotted lines show the location of possible density jumps, reflected as change of slopes in the surface brightness profiles. Lower panels show the residuals of the fit.

Given the limited counts in our short snapshot observation, we fit the surface brightness profiles at projected distance r with a β -model (Cavaliere & Fusco-Femiano 1976)

$$S(r) = S_0 \left[1 + \left(\frac{r}{r_c} \right)^2 \right]^{-3\beta+0.5}, \quad (1)$$

where S_0 is the central X-ray surface brightness and r_c is the core radius. We adopted the IDL package MPFIT (Markwardt 2009), which uses the Levenberg–Marquardt technique to determine the least-squares best fit. Best-fit models are reported as red solid curves in Figure 3, together with best-fit parameters. Residuals are shown in the lower panels of Figure 3.

The F-test was then carried out in order to quantitatively verify whether a two β -model¹⁴ was to be preferred, adopting a significance threshold of 0.05. The two β -model was always rejected, with the exception of the SW sector.

The ICM in galaxy clusters is typically well fitted by models with $\beta \sim 0.6$ (Sarazin 1986; Ettori & Balestra 2009), which steepens with increasing core radius as the two parameters are strongly correlated (Morandi et al. 2015). Our results are in good agreement, as we find that the average surface brightness (azimuthally extracted up to $2'$) is well fitted by a single β -model with $\beta = 0.51 \pm 0.01$. The other three sectors give a rather consistent picture, with β ranging from 0.47 ± 0.01 in the NE sector to 0.56 ± 0.02 in the SE sector. To properly fit the SW profile, we fixed the core radius to $r_{c,1} \sim 15$ kpc (as found from the average azimuthal fit) and $r_{c,2} \sim 135$ kpc, and the resulting best-fitting slopes are $\beta_1 = 0.56 \pm 0.02$, consistent with the fit results of the other four regions, and $\beta_2 = 1.1 \pm 0.1$.

The surface brightness profile, closely tracing the underlying 3D distribution of the gas density, should strictly follow an isothermal profile. Thus a small deviation from the theoretical profile, visible as a change of slope in the surface brightness radial profile, reflects a discontinuity in the underlying gas density. The surface brightness profiles plotted in Figure 3 indeed show these changes of slopes, marked with dotted lines, at ~ 20 kpc, which were already visible as sharp surface brightness “edges” in the central 44×45 kpc² FoV in Figure 2, left panel. There is a discontinuity in the slope of the surface brightness radial profile also in the outer region, around ~ 90 kpc, that was not evident in Figure 2.

To constrain the discontinuity conditions, in the most discrepant cases, e.g., NE and SE, we fit the surface brightness profile within each region assuming spherical symmetry for the gas density and constant gas temperature. The significance of the density discontinuity was quantified by modeling the surface brightness profile across the contact discontinuity with a broken power-law density model (see the appendix of Owers et al. 2009). Given the limited counts of our snapshot observation, we fix the location of the density discontinuity to help the fitting minimization procedure.

For temperatures greater than 2 keV, the discontinuity in the slope of the surface brightness profile is related to the

discontinuity in the gas density as

$$\frac{n_{e,1}}{n_{e,2}} \approx \sqrt{\frac{S_1}{S_2}}, \quad (2)$$

where $n_{e,1}$, $n_{e,2}$ are the densities on either side of the edge, and S_1 , S_2 are the amplitudes of the corresponding surface brightness values. These profiles reveal density ratios of 1.61 ± 0.51 at a distance of 21 kpc, and 1.77 ± 0.30 at a distance of 90 kpc in the SE sector, and 1.80 ± 0.27 at a distance of 85 kpc in the NE region. The position of the outer jumps are quite symmetric between the two sides, since they are at 90 and 85 kpc SE and NE respectively. Assuming the density discontinuities are associated with shocks, the Mach number \mathcal{M} is given by the Rankine–Hugoniot jump condition:

$$\frac{n_{e,d}}{n_{e,u}} = \frac{\gamma + 1}{\gamma - 1 + 2\mathcal{M}^{-2}}, \quad (3)$$

where $n_{e,d}$ and $n_{e,u}$ are the densities downstream and upstream of the shock, respectively. Assuming an ideal gas with ratio of specific heats $\gamma = 5/3$ and the density ratios measured above, the resulting Mach numbers are $\mathcal{M} = 1.42 \pm 0.38$ (SE, $r = 21$ kpc), $\mathcal{M} = 1.54 \pm 0.24$ (SE, $r = 85$ kpc), and $\mathcal{M} = 1.57 \pm 0.22$ (NE, $r = 90$ kpc), which are consistent with a shock origin. We note that by estimating the Mach numbers from the density jumps as shown in Equation (3), we are assuming they are due to shocks. However, it could be that these density discontinuities are caused by sloshing fronts, in which case the temperature discontinuity would be the reciprocal of the density jump. Deeper X-ray observations would certainly clarify the physical origin of the discontinuities.

3.4. Cavities, Asymmetries, and Spiral Features

Surface brightness edges may be caused by at least three phenomena: cold fronts, sloshing of the gas in the central regions of clusters induced by minor mergers, and shocks either AGN- or merger-driven. In particular, gas sloshing is signaled by the presence of a spiral structure in the hot gas distribution (Markevitch & Vikhlinin 2007). To further enhance small-amplitude features in the surface brightness that are otherwise overwhelmed by the gradient associated with the cluster, we adopt two edge-enhancement methods, presented in Figure 4. We caution the reader to not over-interpret the structures in Figure 4. Indeed, the two edge-enhancement methods adopted are inherently noisy and introduce artifacts that complicate quantitative morphological analysis. Figure 4 (particularly the rightmost panel) is presented mostly as a viewing aid for the major morphological features, which are (almost) already visible from the unprocessed data shown in Figure 2.

To highlight the small-scale ripples in the surface brightness, searching for cavities, edges, and sloshing features, we produced a residual image by subtracting a 2D elliptical β -model from the 0.7 to 2 keV *Chandra* image after excising the point sources (see Section 3.1), with native pixel scale $0''.492$, up to $2'$. The left panel of Figure 4 shows the residual image, where regions of surface brightness excess over the subtracted β -model appear in black, whereas deficits are shown in white. The left panel shows the central 20×25 arcsec² (65×80 kpc²) residual image. The butterfly-shaped cavity is clearly seen as a deficit in the residuals.

¹⁴ A two β -model is defined as the linear combination of two different β -models as given in Equation (1).

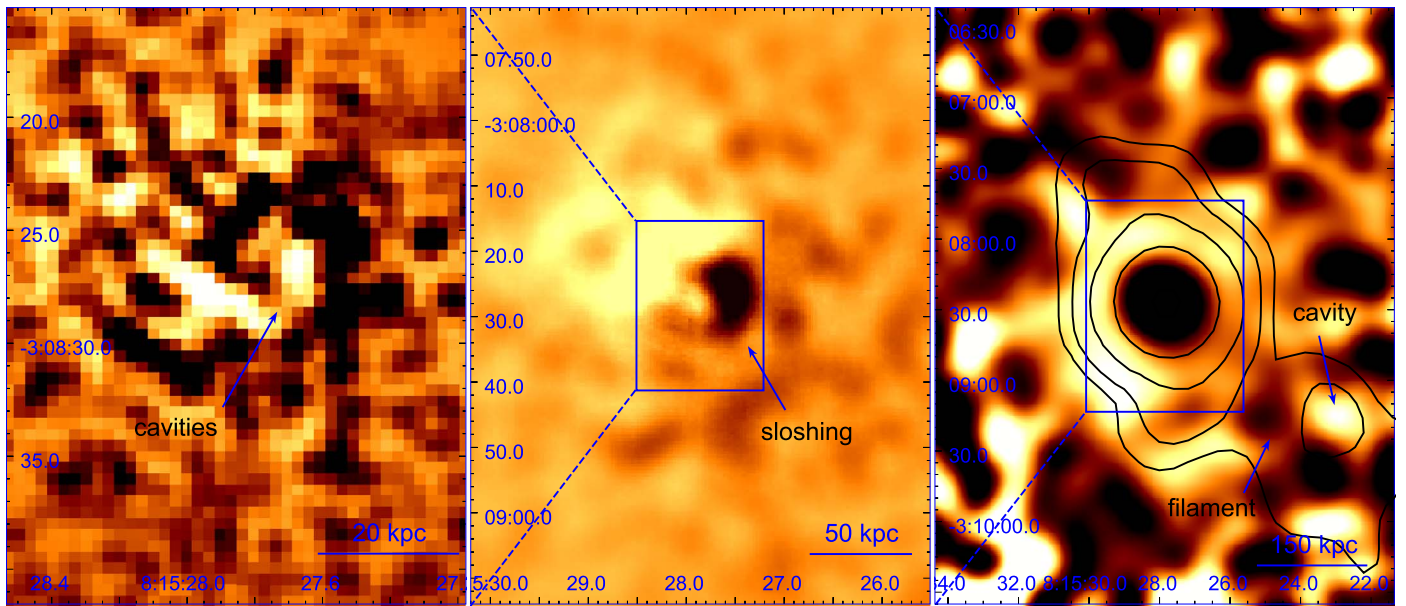


Figure 4. Residuals images of the 0.7–2 keV energy band, with $0''.492$ pixel scale. Excess emission appears in black while depressions are shown in white. Left: residual image produced by the subtraction of a β -model, FoV is 20×25 arcsec 2 (65×80 kpc 2). The butterfly-shaped cavity is clearly seen in the residuals, together with a dark sharp shell that surrounds it. This dark edge is ~ 10 kpc long in projection. Center: the same image is smoothed with a 10 arcsec Gaussian kernel. FoV is $\sim 1 \times 1.5$ arcmin 2 . Asymmetries in the surface brightness are seen together with a spiral feature, indicative of gas sloshing. Right: unsharp mask image produced by the subtraction of 30 arcsec smoothed image from the 15 arcsec smoothed image. The subtracted data are then divided by the sum of the two smoothed images. Field of view is 3×4 arcmin 2 . GMRT 147 MHz contours are overplotted in black (see Figure 2 for details). This edge-enhancement method highlights both the outer cavity, cospatial with the low-frequency radio emission, and the surrounding filament.

The dark sharp region surrounding the cavity to the W, S, and SE is seen as an excess. This edge has a projected radial extent of ~ 10 kpc ($\sim 3''$) with the outer border at a distance of ~ 20 kpc. This is consistent with the first discontinuity in the slope of the surface brightness radial profiles (see dotted lines at ~ 20 kpc in Figure 3).

The central panel shows a larger region, with an FoV of $\sim 1 \times 1.5$ arcmin 2 ($\sim 215 \times 290$ kpc 2). Pixel scale is $0''.492$, smoothed with a Gaussian kernel of $10''$. The Gaussian-smoothed residual image shows asymmetries in the surface brightness. Residual asymmetric features are expected in the case of gas sloshing, and indeed a spiral feature indicative of sloshing is clearly evident both as excess emission (W and S, dark) and deficit (E and N, white). The dark spiral arm is $\sim 6''$ wide and $\sim 12''$ long, which means $\sim 20 \times 40$ kpc 2 .

We also employed an unsharp mask procedure, which is usually adopted as a bandpass spatial filter, in order to enhance structures between the desired spatial scales. The 0.7–2 keV point-source subtracted image is convolved with Gaussian kernels of different sizes. We adopted the kernels of $15''$ and $30''$ to highlight the underlying density discontinuity at ~ 90 kpc indicated by the change of slope in the surface brightness radial profiles in Figure 3. The 30 arcsec smoothed image is subtracted from the 15 arcsec smoothed image and then the subtracted data are divided by the sum of the two images. The right panel of Figure 4 shows the resulting unsharp mask image together with the GMRT 147 MHz contours overlaid in black. The FoV is 3×4 arcmin 2 . Asymmetries in the surface brightness are enhanced even at such scales. The large outer cavity mentioned in Figure 2 is clearly seen in this unsharp masked image, as indicated by the arrow in Figure 4, as well as the filament that surrounds this cavity.

4. Results

4.1. Temperature Gradient

The spectral analysis performed on the *Chandra* data outlined in Section 3.2 implies that the cluster is well fitted by an APEC plasma having ~ 4.2 keV temperature. Inverting the $M_{500}-T$ relation of Lovisari et al. (2015), this temperature corresponds to an $R_{500} \simeq 0.9$ Mpc, which is consistent with the estimate reported by Piffaretti et al. (2011). The temperature analysis shows that the region called *core 1* in Table 1 has a cooler temperature of ~ 3.2 keV. The best-fit gas temperature further drops in the region *core 0*, i.e., considering only the central $10''$, to ~ 2.8 keV.¹⁵ In the four outer sectors (NW, NE, SE, and SW), the best-fit temperatures are higher (at $\gtrsim 2\sigma$ with respect to the region *core 0*). This result suggests that the cluster could be a cool core cluster, with a lower temperature in the central region with respect to the peripheral zones. In the SW direction (coincident with the low-frequency 147 MHz peak emission), there is a hint of a rise in the gas temperature (~ 7.5 keV, see Table 1) with respect to the other three regions. However, this rise in the SW is not statistically significant ($\lesssim 1.5\sigma$), due to the large uncertainties in the best-fit gas temperatures in the cluster outskirts. Indeed, the *Chandra* image has insufficient counts to accurately constrain the temperature in the cluster outskirts, with current 1σ uncertainties of $\sim 20\%$.

4.2. Central Density, Entropy, and Cooling Time

Under the assumption of spherical symmetry and that the projected 2D surface brightness can be described by a β -model

¹⁵ The difference between the two core best-fit temperatures is statistically marginal, $\sim 1\sigma$.

(see Section 3.3), we can derive the underlying 3D electron gas density distribution

$$n_e(r) = n_{e,0} \left[1 + \left(\frac{r}{r_c} \right)^2 \right]^{-\frac{3}{2}\beta}. \quad (4)$$

The central electron density $n_{e,0}$ is obtained using the spectral fit. When fitting a spectrum with an APEC model, the normalization K gives us the electron n_e and proton densities n_p

$$K = \frac{10^{-14}}{4\pi D_A^2 (1+z)^2} \int n_e(r) n_p(r) dV, \quad (5)$$

where D_A is the source angular distance. The normalization in Equation (5) is computed in the volume dV through an infinite cylinder, first integrating radially up to the extraction radius, and then between $-\infty$ and ∞ in order to consider all the emission along the line of sight. Assuming a fully ionized gas, $n_p \simeq 0.82n_e$, we can recover the gas density. The average central density, estimated from the best-fitting parameters of the β -model describing the azimuthal profile inside $2'$ (see bottom panel of Figure 3), is $n_{e,0} \simeq 0.098 \text{ cm}^{-3}$.

We can now estimate the core entropy index, which is defined as $T/n_e^{2/3}$, with the temperature in keV units and the density measured in cm^{-3} . The entropy can be uniquely determined from the entropy index. We use the average temperature of the central region *core 0*, i.e., kT ($r < 10''$) $\simeq 2.8 \text{ keV}$, and the aforementioned estimate of the central density $n_{e,0}$. The resulting core central entropy index is $\sim 13 \text{ keV cm}^2$, and thus the system fits the definition of cool core cluster, taking the characteristic dividing line at $\sim 25 \text{ keV cm}^2$ (Hudson et al. 2010). A low central entropy index value is supported by our analysis that pinpoints a variety of multiphase gas. Indeed, multiphase gas and star formation activity, as hinted, for instance, by the $\text{H}\alpha$ emission (see Figure 1), is expected to be enhanced in BCGs that harbor radio galaxies and with central entropy index below 30 keV cm^2 (Cavagnolo et al. 2008). However, note that the position of the AGN is not obvious, so its contribution to the X-ray emission cannot be subtracted resulting in an overestimate of the X-ray emission, and consequently the central density and entropy. The flux from the cool core contained within $0.15R_{500}$ is $\sim 1.5 \times 10^{-12} \text{ erg cm}^{-2} \text{ s}^{-1}$ in the 0.1–2.4 keV band, corresponding to a luminosity of $\sim 1.5 \times 10^{44} \text{ erg s}^{-1}$. The upper limit on the X-ray nuclear flux (observed-frame and uncorrected for absorption), computed considering all the emission coming from the central circle with radius $2''$, is $\sim 3 \times 10^{-15} \text{ erg cm}^{-2} \text{ s}^{-1}$ in the soft 0.5–1 keV and medium 1–2 keV bands, and $\sim 7 \times 10^{-15} \text{ erg cm}^{-2} \text{ s}^{-1}$ in the hard 2–7 keV band. Nonetheless, the galaxy is classified in the optical as an LERG (Buttiglione et al. 2010), and as such the X-ray emission from the accretion disk is expected to be low (e.g., Hardcastle et al. 2009), hence the AGN X-ray contribution probably does not significantly affect our results.

Additional evidence for a cool core cluster is given by the cooling time

$$t_{\text{cool}} = \frac{3(n_e + n_p)kT}{2\Lambda(T, Z)n_en_p}, \quad (6)$$

where $\Lambda(T, Z)$ is the so-called cooling function, which can be estimated using XSPEC. We found that $\Lambda(kT = 2.8 \text{ keV}$,

$Z = 0.3) \simeq 1 \times 10^{-23} \text{ erg cm}^3 \text{ s}^{-1}$, which gives a cooling time $t_{\text{cool}} \sim 5 \times 10^8$ years (assuming an APEC model with best-fit parameters obtained for the region *core 0*, with 0.3 solar abundance, and a fully ionized gas). The age of the universe at redshift 0.198 is $t_{\text{age}} = 11.122 \times 10^9$ years, thus $t_{\text{cool}}/t_{\text{age}} < 0.05$ supports the cool core nature of the cluster.

4.3. Cavities, Energetics, and Age

Figure 2 shows the 8 ks *Chandra* snapshot observation and the 8.4 GHz radio contours of the core region. There is a wealth of structures already in the snapshot observation, which suggests a complex dynamical state of the system, that could have experienced multiple AGN outbursts. The luminosity L_{500} extrapolated up to R_{500} in the 0.1–2.4 keV band is $\sim 2.8 \times 10^{44} \text{ erg s}^{-1}$, which is consistent with the *ROSAT* measurement (Piffaretti et al. 2011). As already introduced in Section 3.1, in the inner region there is a “butterfly-shaped” cavity wrapping around the SW jet/lobe. The steep (radio) spectrum “S-lobe” impinges on part of this cavity. This system of cavities can be approximated as two contiguous ellipsoids, at a distance $\sim 10 \text{ kpc}$ ($\simeq 3''$), each with a semimajor axis of $2''$ and a semiminor axis of $1''$. To compute the volume, we will assume that the semi axis along the line of sight is the average of the two, i.e., $1.5''$. The resulting volume of each ellipsoid is $1.2 \times 10^{67} \text{ cm}^3$, corresponding to a total cavity volume of $\sim 820 \text{ kpc}^3$.

On large scales, the low-frequency 147 MHz emission extends for hundreds of kiloparsecs to the SW. As already discussed in Section 3.1, this low-frequency radio emission is aligned with the inner scale jet emission. As highlighted in Figure 2, there is a large X-ray filament extending toward the southwest, which spans $\sim 2'$ ($\sim 384 \text{ kpc}$, projected). It could also be the southern border of a large cavity in the hot gas, appearing as a deficit in the X-ray surface brightness, which is cospatial with the peak of 147 MHz radio emission (see Figure 2, right panel). This cavity is marked by a blue dashed ellipsoid with semimajor axis $14''$ and semiminor axis $13''$ (the semi axis along the line of sight is taken $13.5''$). The center of this ellipsoid lies at a (projected) distance of $\sim 90''$ from the AGN. The volume of this cavity would be $\sim 10^{70} \text{ cm}^3$, corresponding roughly to $3 \times 10^5 \text{ kpc}^3$. In both cases, the estimated cavity volumes do not take into account any effect of projection; therefore, they should be considered as upper limits on the real cavity volume. Also, the choice of the semi axis along the line of sight is arbitrary, even though it is consistent with the standard approximation usually adopted in the literature.

The pressure associated with each cavity is given by $P_{\text{cav}} = (n_e + n_p)kT \simeq 1.82n_e(r)kT(r)$. By (i) assuming that the electron density is described by the β -model parameters derived from the azimuthal fit of the region contained in $2'$ (see Figure 3); (ii) assuming a fully ionized gas; and (iii) taking $kT = 2.8 \text{ keV}$ as determined by the spectral fitting in the central $10''$ region (see Table 1) for the inner cavity and instead $kT = 4.2 \text{ keV}$ for the cavity that is located at $\sim 90''$ the resulting pressures are $P_{\text{cav}}^{\text{in}} \simeq 0.5 \text{ keV cm}^{-3}$ for the butterfly-shaped cavity and $P_{\text{cav}}^{\text{out}} \simeq 0.05 \text{ keV cm}^{-3}$ for the outer cavity. Assuming a relativistic plasma, the minimum energy required to create a cavity, e.g., the cavity enthalpy, is

$$E_{\text{cav}} = \frac{\gamma}{\gamma - 1} P_{\text{cav}} V = 4P_{\text{cav}} V, \quad (7)$$

which is $\sim 7 \times 10^{58}$ erg for the inner cavity and $\sim 3 \times 10^{60}$ erg for the outer cavity.

If the low-frequency radio emission comes from a buoyantly rising radio lobe that originated in a past AGN outburst and has displaced the X-ray emitting gas, we can compute its age given its projected clustercentric distance $R \sim 90''$ (~ 290 kpc). Assuming the bubble is launched from the nucleus and rises in the plane of the sky at the sound speed c_s (see, e.g., the review from McNamara & Nulsen 2007)

$$c_s = \sqrt{\frac{kT}{\mu m_p}} \simeq 1100 \left(\frac{kT}{5 \text{ keV}} \right)^{1/2} \text{ km s}^{-1}, \quad (8)$$

where $\mu = 0.62$ is the mean molecular weight in units of the proton mass m_p , and that the ambient temperature at distance R is $kT(R) = 4.2$ keV, then the age of this radio emitting plasma would be

$$t_{\text{rise}} \simeq R/c_s = 280 \text{ Myr}. \quad (9)$$

The simple assumption of a sonic expansion of the bubble does not consider an evolution in the bubble velocity, where the initial stages of the cavity inflation are usually thought to be supersonic and then followed by subsonic buoyant rise. Nonetheless, Equation (9) represents a simple approach that can be used to get an estimate of age average between the two inflation phases.

The age of this radio emission should be of the same order as the AGN radio phase, if this radio emission is related to previous radio outbursts. A timescale of $\sim 10^8$ years is indeed consistent with cycling times between the triggering of radio activity, the onset of quiescence and the subsequent reignition of activity, e.g., 10^7 – 10^8 years (Parma et al. 1999; Best et al. 2005; Shabala et al. 2008; Tremblay et al. 2010). In general, synchrotron losses limit radio source lifetimes to $\sim 10^8$ years in a few μG magnetic field typical of lobes in radio galaxies, unless there has been reacceleration of the electron population.

We can estimate the same quantities also for the inner cavity, at a distance of ~ 10 kpc, assuming that the temperature inside the cavity is given by the average temperature $kT \sim 2.8$ keV we found in the region *core 0*. We then get an age of ~ 12 Myr.

We can finally compute the jet power P_{jet} , which is the minimum work required to inflate a cavity with a volume V , i.e., the cavity enthalpy in Equation (7), divided by the age of the cavity,

$$P_{\text{jet}} = 4PV/t = E_{\text{cav}}/t. \quad (10)$$

As shown in Equation (9), the cavity age can be approximated by the bubble rise time, under the (simplistic) assumption of sonic expansion. The resulting jet powers are $\sim 1.9 \times 10^{44}$ erg s^{-1} for the inner cavity and $\sim 3.4 \times 10^{44}$ erg s^{-1} , which are consistently measured also in other galaxy clusters (see the review of Bykov et al. 2015, their Figure 7).

5. Summary and Conclusions







Performing a multiwavelength analysis from publicly available radio, optical, and X-ray images, we have investigated the nature of the multiphase emitting gas both in the nuclear and surrounding regions of 3C 196.1. The emerging scenario is that this radio galaxy could have undergone several radio outbursts on multiple epochs and its cluster may have experienced a merger. In particular:

1. Optical *HST* observations reveal clear signs of interactions between the radio jet and lobe with the $\text{H}\alpha$ + $[\text{N II}]$ emitting gas. Distortions in the optical isophotes of the BCG support a scenario of merging. In Figure 1, there is filamentary $\text{H}\alpha$ + $[\text{N II}]$ emission extending eastward, draped across the radio lobe. This $\text{H}\alpha$ + $[\text{N II}]$ filament must be dynamically very short lived. Indeed, recombination times for $T \sim 10^4$ K gas are of order 10^3 years (Osterbrock & Ferland 2006), while lifetimes of radio sources are of order 10^8 years. The process by which the $\text{H}\alpha$ + $[\text{N II}]$ gas is ionized should therefore be ongoing throughout the lifetime of the radio source. This implies a strong connection between AGN activity and observed emission line properties.
2. The low-frequency and high-frequency radio data helped us to investigate both the inner and outer scales of the cluster. By comparing the galactic-scale radio and *HST* images, we have found that the $\text{H}\alpha$ + $[\text{N II}]$ emission is aligned with the inner scale jet, an example of the well-known ‘‘alignment effect’’ (Fosbury 1986; Hansen et al. 1987; Baum et al. 1988, 1990; de Vries et al. 1999; Tremblay et al. 2009). The combination of the radio and the X-ray images allowed us to discover cavities located in the galaxy, at ~ 10 kpc, and in the cluster outskirts, at ~ 290 kpc, whose presence suggests past AGN outbursts.
3. The $\text{H}\alpha$ + $[\text{N II}]$ emission is bounded to the SW by the butterfly-shaped cavity in the inner region and the filamentary emission to the NE is cospatial with the northern hotspot.
4. The *Chandra* X-ray data analysis allowed us to constrain basic physical parameters of the cluster and of the ICM gas. We revealed the presence of discontinuities in the gas density by analyzing the surface brightness profiles. Assuming these discontinuities are due to shocks, we determined the Mach numbers from the density jumps, derived under the Rankine–Hugoniot conditions. The inferred Mach numbers and density jumps are consistent with having originated from shocks. We also employed two different edge-enhancement methods to better visualize the small ripples in surface brightness associated with density discontinuities. In this way, we found a spiral pattern, characteristic of gas sloshing, suggesting a past merger event.
5. We found a decrease in temperature in the inner region, suggesting that 3C 196.1 is hosted in a cool core cluster. This result is further supported by the analysis of the X-ray surface brightness, through which we determined the core entropy index of ~ 13 keV cm^2 and the cooling time $t_{\text{cool}} \sim 500$ Myr.
6. Finally, we computed the volumes, pressures, and enthalpies E_{cav} associated with the cavities: $E_{\text{cav}} \sim 7 \times 10^{58}$ erg for the inner cavity and $E_{\text{cav}} \sim 3 \times 10^{60}$ erg for the outer cavity. We also determined the lifetimes of both cavities, the inner cavity of ~ 12 Myr and the outer one of ~ 280 Myr, by assuming that the radio plasma is a sonic rising bubble. This lifetime is consistent with radio cycle lifetimes and thus supports the origin of the outer cavity as a past AGN outburst. With the estimate of bubble rise time, we computed the jet powers P_{jet} and found $P_{\text{jet}} \sim 1.9 \times 10^{44}$ erg s^{-1} for the inner cavity and $P_{\text{jet}} \sim 3.4 \times 10^{44}$ erg s^{-1} for the outer cavity.

Given that the $H\alpha$ +[N II] gas filaments are aligned with the radio jets/bubbles, we are probably witnessing an example here of lobes uplifting cold gas, even though robust conclusions cannot be drawn since we do not have any kinematic information. Deeper X-ray and radio data would be critical to provide clues about the dynamics of the cold and hot phase gas, and to obtain a more complete understanding of the morphology and of the nature of the system. Additional deeper data would also be needed to better define cavities, constrain the temperature and metallicity distributions, and look for additional merger features. This source thus represents an intriguing opportunity to quantify, with deeper X-ray observations, the impact of AGN activity in the outskirts of a group in a nearby cluster.

We thank the referee for valuable suggestions that improved the quality of the manuscript. We acknowledge C. C. Cheung for kindly providing the 8.4 GHz radio map. This investigation is supported by the National Aeronautics and Space Administration (NASA) grants GO4-15096X, GO4-15097X, and GO6-17081X. F.R. acknowledges support from FONDECYT Postdoctorado 3180506 and CONICYT project Basal AFB-170002. L.L. acknowledges support from NASA through contract NNX17AD83G. This work is supported by the “Departments of Excellence 2018-2022” Grant awarded by the Italian Ministry of Education, University and Research (MIUR) (L. 232/2016). This research has made use of resources provided by the Compagnia di San Paolo for the grant awarded on the BLENV project (S1618_L1_MASF_01) and by the Ministry of Education, Universities and Research for the grant MASF_FFABR_17_01. F.M. acknowledges financial contribution from the agreement ASI-INAF n.2017-14-H.0. The work of S.B. and C.O. was supported by NSERC (Natural Sciences and Engineering Research Council of Canada). This research has made use of NASAs Astrophysics Data System; SAOImage DS9, developed by the Smithsonian Astrophysical Observatory, and the NASA/IPAC Extragalactic Database (NED), which is operated by the Jet Propulsion Laboratory, California Institute of Technology, under contract with the National Aeronautics and Space Administration. The (USA) National Radio Astronomy Observatory (NRAO) is operated by Associated Universities, Inc., and is a Facility of the (USA) National Science Foundation. We thank the staff of the GMRT that made these observations possible. GMRT is run by the National Centre for Radio Astrophysics of the Tata Institute of Fundamental Research. Facilities: VLA, GMRT, *HST*, CXO (ACIS).

ORCID iDs

F. Ricci  <https://orcid.org/0000-0001-5742-5980>
 L. Lovisari  <https://orcid.org/0000-0002-3754-2415>
 R. P. Kraft  <https://orcid.org/0000-0002-0765-0511>
 F. Massaro  <https://orcid.org/0000-0002-1704-9850>
 A. Paggi  <https://orcid.org/0000-0002-5646-2410>
 G. Tremblay  <https://orcid.org/0000-0002-5445-5401>
 W. R. Forman  <https://orcid.org/0000-0002-9478-1682>
 C. O’Dea  <https://orcid.org/0000-0001-6421-054X>
 B. Wilkes  <https://orcid.org/0000-0003-1809-2364>

References

- Arnaud, K. A. 1996, in ASP Conf. Ser.101, *Astronomical Data Analysis Software and Systems V*, ed. G. H. Jacoby & J. Barnes (San Francisco, CA: ASP), 17
- Asplund, M., Grevesse, N., Sauval, A. J., & Scott, P. 2009, *ARA&A*, 47, 481
- Baum, S. A., & Heckman, T. 1989, *ApJ*, 336, 681
- Baum, S. A., Heckman, T., & van Breugel, W. 1990, *ApJS*, 74, 389
- Baum, S. A., Heckman, T. M., Bridle, A., van Breugel, W. J. M., & Miley, G. K. 1988, *ApJS*, 68, 643
- Begelman, M. C., & Nath, B. B. 2005, *MNRAS*, 361, 1387
- Bennett, A. S. 1962, *MNRAS*, 125, 75
- Best, P. N., Kauffmann, G., Heckman, T. M., & Ivezić, Ž. 2005, *MNRAS*, 362, 9
- Best, P. N., Röttgering, H. J. A., & Longair, M. S. 2000, *MNRAS*, 311, 23
- Birzan, L., McNamara, B. R., Nulsen, P. E. J., Carilli, C. L., & Wise, M. W. 2008, *ApJ*, 686, 859
- Blanton, E. L., Randall, S. W., Clarke, T. E., et al. 2011, *ApJ*, 737, 99
- Boehringer, H., Voges, W., Fabian, A. C., Edge, A. C., & Neumann, D. M. 1993, *MNRAS*, 264, L25
- Buttiglione, S., Capetti, A., Celotti, A., et al. 2010, *A&A*, 509, A6
- Bykov, A. M., Churazov, E. M., Ferrari, C., et al. 2015, *SSRv*, 188, 141
- Cavagnolo, K. W., Donahue, M., Voit, G. M., & Sun, M. 2008, *ApJL*, 683, L107
- Cavagnolo, K. W., McNamara, B. R., Nulsen, P. E. J., et al. 2010, *ApJ*, 720, 1066
- Cavaliere, A., & Fusco-Femiano, R. 1976, *A&A*, 49, 137
- Churazov, E., Brügggen, M., Kaiser, C. R., Böhringer, H., & Forman, W. 2001, *ApJ*, 554, 261
- Churazov, E., Forman, W., Jones, C., & Böhringer, H. 2000, *A&A*, 356, 788
- Churazov, E., Ruszkowski, M., & Schekochihin, A. 2013, *MNRAS*, 436, 526
- de Koff, S., Baum, S. A., Sparks, W. B., et al. 1996, *ApJS*, 107, 621
- de Vries, W. H., O’Dea, C. P., Baum, S. A., & Barthel, P. D. 1999, *ApJ*, 526, 27
- Dopita, M. A., & Sutherland, R. S. 1995, *ApJ*, 455, 468
- Dopita, M. A., & Sutherland, R. S. 1996, *ApJS*, 102, 161
- Dunkley, J., Komatsu, E., Nolta, M. R., et al. 2009, *ApJS*, 180, 306
- Ettori, S., & Balestra, I. 2009, *A&A*, 496, 343
- Fabian, A. C. 2012, *ARA&A*, 50, 455
- Fanaroff, B. L., & Riley, J. M. 1974, *MNRAS*, 167, 31P
- Forman, W., Churazov, E., Jones, C., et al. 2017, *ApJ*, 844, 122
- Fosbury, R. A. E. 1986, *ASSL*, 121, 297
- Fruscione, A., McDowell, J. C., Allen, G. E., et al. 2006, *Proc. SPIE*, 6270, 62701V
- Gaspari, M., Brighenti, F., & Temi, P. 2015, *A&A*, 579, A62
- Gitti, M., Brighenti, F., & McNamara, B. R. 2012, *AdAst*, 2012, 950641
- Gopal-Krishna, & Wiita, P. J. 2000, *A&A*, 363, 507
- Hansen, L., Jorgensen, H. E., & Norgaard-Nielsen, H. U. 1987, *A&AS*, 71, 465
- Hardcastle, M. J., Evans, D. A., & Croston, J. H. 2009, *MNRAS*, 396, 1929
- Hudson, D. S., Mittal, R., Reiprich, T. H., et al. 2010, *A&A*, 513, A37
- Intema, H. T., Jagannathan, P., Mooley, K. P., & Frail, D. A. 2017, *A&A*, 598, A78
- Jones, C., Forman, W., Vikhlinin, A., et al. 2002, *ApJL*, 567, L115
- Kaiser, C. R., & Best, P. N. 2007, *MNRAS*, 381, 1548
- Kapińska, A. D., Terentev, I., Wong, O. I., et al. 2017, *AJ*, 154, 253
- Kharb, P., Lister, M. L., & Cooper, N. J. 2010, *ApJ*, 710, 764
- Kocevski, D. D., Ebeling, H., Mullis, C. R., & Tully, R. B. 2007, *ApJ*, 662, 224
- Lovisari, L., Reiprich, T. H., & Schellenberger, G. 2015, *A&A*, 573, A118
- Madrid, J. P., Chiaberge, M., Floyd, D., et al. 2006, *ApJS*, 164, 307
- Main, R. A., McNamara, B. R., Nulsen, P. E. J., Russell, H. R., & Vantyghem, A. N. 2017, *MNRAS*, 464, 4360
- Markevitch, M., & Vikhlinin, A. 2007, *PhR*, 443, 1
- Markwardt, C. B. 2009, in ASP Conf. Ser.411, *Astronomical Data Analysis Software and Systems XVIII*, ed. D. A. Bohlender, D. Durand, & P. Dowler (San Francisco, CA: ASP), 251
- Massaro, F., Harris, D. E., Liuzzo, E., et al. 2015, *ApJS*, 220, 5
- Massaro, F., Harris, D. E., Tremblay, G. R., et al. 2010, *ApJ*, 714, 589
- Massaro, F., Harris, D. E., Tremblay, G. R., et al. 2013, *ApJS*, 206, 7
- Massaro, F., Missaglia, V., Stuardi, C., et al. 2018, *ApJS*, 234, 7
- Massaro, F., Tremblay, G. R., Harris, D. E., et al. 2012, *ApJS*, 203, 31
- McNamara, B. R., Kazemzadeh, F., Rafferty, D. A., et al. 2009, *ApJ*, 698, 594
- McNamara, B. R., & Nulsen, P. E. J. 2007, *ARA&A*, 45, 117
- Morandi, A., Sun, M., Forman, W., & Jones, C. 2015, *MNRAS*, 450, 2261

- Osterbrock, D. E., & Ferland, G. J. 2006, *Astrophysics of Gaseous Nebulae and Active Galactic Nuclei* (2nd ed.; Sausalito, CA: Science Books)
- Owers, M. S., Nulsen, P. E. J., Couch, W. J., & Markevitch, M. 2009, *ApJ*, **704**, 1349
- Parma, P., Murgia, M., Morganti, R., et al. 1999, *A&A*, **344**, 7
- Piffaretti, R., Arnaud, M., Pratt, G. W., Pointecouteau, E., & Melin, J.-B. 2011, *A&A*, **534**, A109
- Randall, S. W., Nulsen, P. E. J., Jones, C., et al. 2015, *ApJ*, **805**, 112
- Sarazin, C. L. 1986, *RvMP*, **58**, 1
- Scannapieco, E., Silk, J., & Bouwens, R. 2005, *ApJL*, **635**, L13
- Shabala, S. S., Ash, S., Alexander, P., & Riley, J. M. 2008, *MNRAS*, **388**, 625
- Spinrad, H., Marr, J., Aguilar, L., & Djorgovski, S. 1985, *PASP*, **97**, 932
- Stuardi, C., Missaglia, V., Massaro, F., et al. 2018, *ApJS*, **235**, 32
- Su, Y., Nulsen, P. E. J., Kraft, R. P., et al. 2017, *ApJ*, **847**, 94
- Tremblay, G. R., Chiaberge, M., Sparks, W. B., et al. 2009, *ApJS*, **183**, 278
- Tremblay, G. R., O’Dea, C. P., Baum, S. A., et al. 2010, *ApJ*, **715**, 172
- Tremblay, G. R., O’Dea, C. P., Baum, S. A., et al. 2012, *MNRAS*, **424**, 1026
- Zirbel, E. L. 1996, *ApJ*, **473**, 713